



Effects of Ti and Al incorporation on the performance of FSM-16 supported nickel catalyst in dry reforming of methane

Rezvan Rafieenezhad¹ · Ali Izadbakhsh¹ · Ali Mohammad Sanati²

Accepted: 16 June 2021

© The Author(s), under exclusive licence to Springer Science+Business Media, LLC, part of Springer Nature 2021

Abstract

The effect of Ti and Al incorporation to FSM-16 framework as the support of Ni catalysts on their catalytic performance in the reaction of dry reforming of methane (DRM) was investigated. A series of Ni/M-FSM-16 ($M = Al, Ti$) with M/Si molar ratio = 100, 50, 20 were synthesized via double-solvent impregnation of Nickel. Fresh catalysts were characterized using N_2 adsorption/desorption, XRD, FTIR, FE-SEM, H_2 -TPR analyses. The prepared catalyst went through DRM reaction at 750, 800, and 850 °C. The spent catalysts of best catalytic performance, i.e. Ni/ Al_{50} -FSM-16 and Ni/ Ti_{100} -FSM-16, were analyzed by FT-IR and O_2 -TPO to characterize carbonaceous deposits. Based on TPR results, the promotion of DRM performances was related to the strength of Ni interaction with supports to which Ti or Al was incorporated. Conversion of CH_4 and CO_2 , and H_2/CO ratio of the products via Ni/ Al_{50} -FSM-16 catalyst were promoted by 95%, 83%, 25% with respect to Ni/FSM-16 at 850 °C, respectively.

Keywords FSM-16 · Nickel · Mesoporous Silica · Catalyst · Reforming · CO_2

1 Introduction

The growth of the world's population along with the increase in human need for energy raises serious environmental concerns. One of these concerns is global warming, a phenomenon that results from the emission of large amounts of greenhouse gases in the Earth's atmosphere due to the high consumption of fossil fuels [1, 2]. The reduction of these gases, which mostly are Carbon dioxide (CO_2) and Methane (CH_4), is a necessary and important issue that needs to be taken into consideration. On the other hand, among the alternative and renewable energies, hydrogen, with the highest theoretical specific energy in comparison to other known fuels, is an economic and clean energy resource. In order to sustain industrial and economic development, natural gas,

which is mostly methane, can be converted to hydrogen by catalytic chemical conversion [3, 4].

The catalytic conversion of methane occurs via several reactions such as steam reforming of methane (SMR), partial oxidation of methane (PMO), dry reforming of methane (DRM) and hybrid reforming (as autothermal reforming (ATR) and tri-reforming) [5] that mainly lead to production of the synthesis gas (syngas) as a valuable petrochemical feedstock. The advantages of dry reforming of methane to others are the consumption of two greenhouse gases (CH_4 and CO_2) and production of the syngas with a favorable H_2/CO ratio for its application in the Fisher-Tropsch process. It removes the pre-treatment unit in GTL technology and reduces the operating cost of the production of dimethyl ether, olefins and aromatics [5].

Despite these advantages, the presence of some side reactions that occur simultaneously with DRM reaction causes the deviation of H_2/CO molar ratio from 1 which also leads to the deactivation of supported metal catalysts by carbon deposition. These disadvantages could significantly be reduced by using precious metals-based catalysts but their scarcity and high prices caused the DRM process to be non-commercialized in industrial utilization. However, replacing the transition metals such as Ni can partly solve these problems.

✉ Ali Izadbakhsh
izadbakhsh@pgu.ac.ir

¹ Department of Chemical Engineering, Faculty of Petroleum, Gas and Petrochemical Engineering, Persian Gulf University, P.B. 75169-13817, Bushehr, Iran

² Department of Environmental Science, Persian Gulf Research Institute, Persian Gulf University, P.B. 75169-13817, Bushehr, Iran

Applying materials of various compositions and structures as the supports of active metals is a very challenging issue, because the well dispersion of the active metal is directly related to the high surface area of the support [6]. Therefore, numerous supports such as single oxides (Al_2O_3 , SiO_2 , ZrO_2), mixed metal oxides (spinel, perovskites, $\text{Ce}_{0.6}\text{Zr}_{0.4}\text{O}_2$, $\text{La}_2\text{O}_3\text{--CeO}_2\text{--ZrO}_2$, $\text{Gd}_{0.1}\text{Ti}_{0.1}\text{Zr}_{0.1}\text{Ce}_{0.7}\text{O}_2$), zeolites, clays, carbon-based materials and mesostructured materials (ordered mesoporous silica, e.g. SBA-15, MCM-41, KIT-6) have been investigated as the supports of the DRM catalysts [7, 8]. Among these materials, ordered mesoporous silica have large pore volumes, high specific surface areas, interconnected porous framework with uniform and tunable pore size distribution. These siliceous materials are specially able to replace their silica atoms when incorporated with other metals such as Al, Zr, Sn inside the matrix [7, 9].

Dry reforming of methane over ordered mesoporous silica supported Ni catalysts has been investigated by many researchers [10–18]. The catalytic activity of Ni/Mg-SBA-15 was increased owing to the enhancement of basic sites of SBA-15 by adding Mg atoms. Ni dispersion was promoted and resistance to Ni sintering and coke formation were increased dramatically [14]. The effect of strong metal-support interaction by incorporating several transition metals into the silica network of MCM-41 was also studied. Comparison of Mn, Ti and Zr modified catalysts indicated high catalytic activity and long-term stability. Existence of Zr in the support structure improved the thermal stability of the MCM-41 silica framework. The stronger anchoring effect of Zr^{4+} and partial activation of CO_2 with Zr^{4+} species led to the good dispersion of Ni nanoparticles with excellent performance in DRM reaction [19]. It was reported that the altering of support acidity by introduction of Al and Na in the MCM-41 framework demonstrated very different results. Although increasing support acidity by incorporating Al and/or decreasing the acidity by entrapping Na ions reduced CH_4 conversion of Ni/MCM-41, carbon accumulation was unexpectedly suppressed at high acidity conditions by Al incorporation and Na inclusion enhanced RWGS reaction with overall less coke formation relative to neat MCM-41 supported nickel. These effects were related to the impact of Na exchange on Ni particle size. Therefore, the stability and selectivity of the catalysts can be controlled by adjusting the acidity of support [20]. In a recent study about promotion of the support properties, an aluminum-modified SBA-15 (Al-SBA-15) was prepared to enhance the sintering resistance and hydrothermal stability of the Ni embedded Al-SBA-15 catalyst. The researchers claimed that the confinement effect of SBA-15 channels with superior hydrothermal stability arose from Al incorporation raised the performance of the catalyst. In addition, whenever ethylene glycol (EG) was used as the solvent of nickel solution in the impregnation

step to effectively deliver Ni ions into the mesochannels, very fine Ni particles were formed and contributed to the enhancement of the DRM reaction [21].

FSM-16 is one of the oldest members of the ordered mesoporous silica family prepared from a layered hydrated sodium silicate named kanemite ($\text{NaHSi}_2\text{O}_5\text{.3H}_2\text{O}$). Its structure is very similar to MCM-41 and both have two-dimensional regular honeycomb arrays consisting of non-cross cylindrical pores. However, FSM-16 has different pore wall structures and surface properties owing to its various formation mechanisms that could lead to different catalytic yields [22–26]. Direct substitution of metals into silica framework of FSM-16 is performed by adding the metal source in the kanemite preparation stages, i.e. during the step of sodium silicate synthesis ($\delta\text{-Na}_2\text{Si}_2\text{O}_5$). Synthesis of Al-FSM-16, Sn-FSM-16 and Zr-FSM-16 using Al-, Sn- and Zr-containing $\delta\text{-Na}_2\text{Si}_2\text{O}_5$ was reported in literature [27–30]. Insertion of aluminum into the FSM-16 matrix enhanced the acidic properties and hydrothermal stability of the Al-FSM-16 samples as the catalyst of the isomerization of m-xylene reaction. The acidity of the catalyst was an effective factor on the catalytic conversion and deactivation of the catalyst [29]. Al-FSM-16 was also prepared in two ways, i.e. direct and post-synthesis, and was used in the catalytic decomposition of ethanol as a sensitive reaction to the acid-base properties of the employed catalyst. This reaction produces ethylene and diethyl ether on the acidic catalyst and/or acetaldehyde on basic/redox centers. The directly Al incorporated FSM-16 had less acidic strength than others and mostly generated acetaldehyde [30]. On adding transition metals into the FSM-16 framework, the catalytic properties of Zr-incorporated FSM-16 supported Co catalyst were investigated in the Fischer-Tropsch (F-T) synthesis. The researchers realized that Zr^{4+} probably provided strong interaction with Co sites and that Co/Zr-FSM-16 showed higher catalytic activity than Co/FSM-16. The Co_3O_4 particles were reduced at lower temperature and the Zr^{4+} had a positive effect as a co-catalyst in F-T synthesis [28].

It should be noted that in addition to the study of supports and promoting their properties, developing methods to obtain high metal dispersion is a key challenge in the design of supported metal catalysts. In a common impregnation method, the large particles could be formed and distributed with an unfavorable dispersion mostly on the external surface of support [31–33]. A new technique called “double solvent” impregnation method has been found to facilitate the homogeneous dispersion of metal oxide mainly on the internal surface of pores. The strategy is that a hydrophobic solvent contributes in the uniform and homogeneous penetration of metal aqueous solution by pre-wetting and filling the hydrophilic channels [34–38]. This technique has been applied to achieve highly active and stable Ni/SBA-15 catalysts for the DRM process. By double-solvent

impregnation, the sintering of Ni nanoparticles was inhibited and the coke deposition was remarkably diminished [39]. The performance of several catalysts impregnated by this procedure was evaluated in the syngas methanation reaction. It was illustrated that the greater number of active sites with stronger metal-support interaction and thermal resistance than traditional impregnation led to higher CO conversion and CH₄ yield. According to the characterization results of spent catalysts, despite good dispersion of active metals, sintering of Ni nanoparticles was the major reason of deactivation compared to coke formation under reaction conditions [40].

In this work, the catalytic performance of a series of Ni catalysts, supported on mesoporous FSM-16 silica to which Al or Ti was incorporated in the dry reforming of methane, was compared. Al and Ti were incorporated into the FSM-16 silica matrix in order to promote the thermal strength of Ni/FSM-16 catalysts, the dispersion of Ni nanoparticles, and overall catalytic performance. To determine the optimal range of incorporated metal content, different molar ratios were added to the synthesis batch. Herein, double solvent impregnation was employed to obtain fine Ni particles with enhanced catalytic activity as much as possible.

2 Experimental

2.1 Catalyst preparation

2.1.1 Synthesis of FSM-16, Al-FSM-16 and Ti-FSM-16 supports

According to the FSM-16 synthesis method reported by Inagaki et al. [41], 3.8 g NaOH was dissolved in 100 mL deionized water and 6 g of fumed silica was added to the solution. The FSM-16 product was obtained after stirring the mixture for 3 h, drying at 100 °C by a rotary evaporator followed by calcination at 700 °C for 6 h. To incorporate the Al atoms in the FSM-16 silicate framework, the predetermined amount of Al(NO₃)₃.9H₂O (Si/Al = 100, 50 and 20) was dissolved in 5 ml of water and the solution was added dropwise into the mixture of NaOH and SiO₂ after about 45 min of stirring. To synthesize Ti incorporated FSM-16 silica, the required amount of Ti(OBu)₄ to obtain Si/Ti ratios = 100, 50 and 20 was dissolved in 5 ml of isopropanol and added to the mixture of NaOH and SiO₂. To keep (Si + M)/Ni constant in every synthesis mixture of M-incorporated support with Si/M ratio = 100, 50, 20 the amount of fumed silica used in each synthesis was adjusted. The remaining steps explained in the following was the same for the synthesis of FSM-16, Al-FSM-16, and Ti-FSM-16 silica.

To achieve the kanemite paste and exchange Na⁺ with H⁺ cations, the obtained powders were immersed in the

deionized water and stirred for 3 h at 27 °C. Afterwards, it was added to an aqueous solution of cetyltrimethylammonium bromide (CTAB, 0.125 mol L⁻¹) and the mixture was heated up to 70 °C with stirring for 3 h at the adjusted pH 11.5.

Then, the pH of the solution was declined to 8.5 by addition of 2 mol.L⁻¹ HCl and the mixture was stirred for another 3 h at the same temperature. After filtration, washing with water and drying the resulting gel, it was finally treated with ethanol and calcined at 550 °C for 12 h. The obtained solids were denoted as FSM-16, Al-FSM-16 or Ti-FSM-16 [42].

2.1.2 Synthesis of Ni/FSM-16, Ni/Al-FSM-16 and Ni/Ti-FSM-16 catalysts

The double-solvent impregnation method has been employed to prepare the nickel catalysts. 1.0 g of FSM-16, Al-FSM-16 or Ti-FSM-16 powder was dispersed in 20 mL n-hexane and stirred for 2 h at ambient temperature. 0.57 g of Ni(NO₃)₂.6H₂O (Ni = 10.2 wt%) was dissolved in 1.14 ml of distilled water followed by dropwise addition of the latter aqueous solution of nickel nitrate into the suspension and the mixture was stirred for 3 h. Then, final products were dried in air for 24 h and calcined at 550 °C for 5 h under argon stream [43].

2.2 Catalyst characterization

The structural and textural properties of the synthesized supports and catalysts were analyzed by X-ray diffraction, Nitrogen adsorption–desorption isotherms, Field emission scanning electron microscopy (FESEM), Fourier transform infrared spectroscopy (FTIR), Temperature programmed reduction (H₂-TPR) and Temperature programmed oxidation (O₂-TPO) analyses.

Crystalline phase of the prepared catalysts was analyzed through their XRD patterns recorded via Philips PW1730 diffractometer equipped with a Cu K α ($\lambda=0.154$ nm) radiation running with the power of 1200 watts (40 keV). The XRD spectra was scanned angular range 0.8–10 for small angle mode (step size is 0.02°/min) and 10–80 in wide angle mode (step size is 0.05°/min). N₂ adsorption–desorption isotherms were obtained at liquid nitrogen temperature = –196 °C via micromeritics ASAP 2020 surface analyzer instrument. The Brunauer–Emmett–Teller (BET) method and Barrett–Joyner–Halenda (BJH) theory were adopted to calculate surface area, specific pore volume and pore size distribution of the catalysts.

The elemental linkage information was studied by FTIR spectra of catalysts recorded via Broker Tensor 27 FTIR spectrometer in wavenumber span of 400–4000 cm⁻¹. FESEM images were recorded via TESCAN MIRA III to

identify crystallites size and particles morphology. The H₂-TPR profiles of fresh catalysts were collected utilizing the laboratory reactor setup used for the evaluation of catalytic performance. The sample were treated in a U-shaped quartz tube where the outlet gas flow was directed to a thermal conductivity detector (TCD). After degassing 0.1 g of sample at 300 °C for 1 h with Ar flow = 30 ml/min, it was cooled down to 100 °C in about 2 h and then was heated to 850 °C with the ramp of 10 °C/min under H₂/Ar (10 vol%) gas flow of 30 ml/min. The amount of H₂ uptake was monitored with time by signal of TCD.

To reveal the types and amount of carbon deposited on the catalysts during DRM reaction, the spent catalysts underwent TPO experiment carried out on the same reactor setup. Samples were pretreated at 200 °C for 1 h under Ar stream, followed by rising temperature to 850 °C with a ramp of 10 °C/min in O₂/Ar flow = 32 mL/min.

2.3 Catalytic activity test

In a typical experiment, 0.2 g of catalyst particles was mixed with 0.2 g of quartz sand and packed between two layers of 0.4 g of quartz sand in a U-shaped quartz tube to ensure a uniform heated gas flow through the nearly isothermal catalyst bed. All particles were sieved to 20–30 mesh size. In a typical experiment, the catalyst sample was reduced under a flow of a mixed stream of H₂/Argon (H₂/Ar = 10/40 ml/min) by heating to 750 °C at the rate of 10 °C/min and hold time = 2 h. Then, DRM Reaction was started with the introduction of equimolar streams (30/30 ml/min) of CH₄ and CO₂ at the temperatures of 750, 800 and 850 °C, sequentially. Reaction at each temperature was continued for about 2 h. The outlet flow, after passing through a vapor trap, were analyzed by Agilent 7890 gas chromatograph (GC) equipped with a TCD detector and thin film HP-PLOT Q capillary column of length = 30 m and inner diameter = 0.53 mm under He flow as carrier gas. In each GC analysis of product samples, the oven temperature was kept isothermal at 35 °C, the injection temperature was 120 °C, and the temperature of TCD detector was set to 150 °C.

3 Results and discussion

3.1 Characterization of support samples and fresh catalyst

3.1.1 Small angle X-ray diffraction

To verify the formation of crystalline lattice of the mesopore structure of supports, small angle XRD patterns were collected for each sample. As shown in Fig. 1, the XRD pattern was in agreement with the literature. There are four

distinct peaks for FSM-16 at $2\theta = 2\text{--}7^\circ$, proving the formation of highly ordered mesoporous silica. The first peak at $2\theta = 2.47$ was assigned to the crystallographic plane (100) and the others at $2\theta = 4.10, 4.73$ and 6.25 were related to Bragg's reflections of planes (110), (200) and (210), respectively. Accordingly, the crystalline network with two-dimensional (2-D) hexagonal pore structure of the synthesized FSM-16 were confirmed.

The small angle XRD profiles of Al-containing FSM-16 silicas with different content of aluminum, given in Fig. 1, indicated that the intensity of XRD peaks decreased with Al content as well as a slight shift of the first strong peak to larger 2θ for Al₅₀FSM-16 and a reverse shift for Al₂₀FSM-16 with respect to Al₁₀₀FSM-16.

The d-spacing of plane (100) of mesopores in Al₁₀₀FSM-16 was very close to that of FSM-16 (35.7 Å), however, it decreased to 34.3 Å by increasing Al content (Si/Al = 50), followed by increasing to 38 Å with a further increase of Al incorporation (Si/Al = 20). It indicates that Al incorporation can change the lattice parameter of the mesopore structure in FSM-16.

The XRD patterns of Ti incorporated samples, shown in Fig. 1, confirmed the hexagonal order of pore structures in FSM-16. The strong reflection of plane (100) at $2\theta = 2.32$ was observed in all the XRD patterns and two other minor peaks of lattice plane (110) and (200) were clear in the spectrum of Ti₁₀₀FSM-16. These two peaks lost their strength in the spectrum of the other samples with higher Ti content. The reflection of plane (100) in all as-prepared Ti incorporated mesoporous FSM-16 exhibited a weak shift to smaller 2θ s ($\Delta = 0.15$ Å) with respect to that of FSM-16. However,

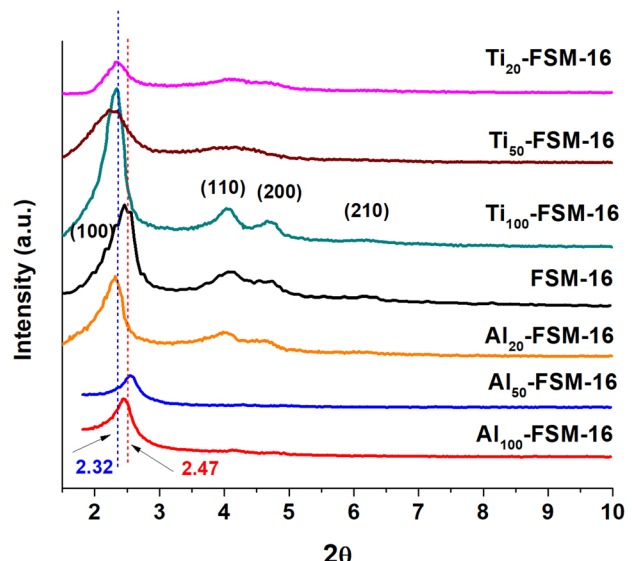


Fig. 1 Small angle XRD pattern of FSM-16 support and the modified supports

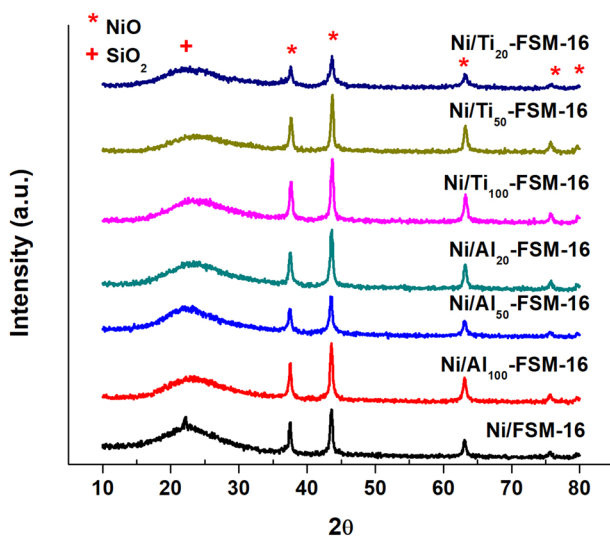


Fig. 2 Wide angle XRD patterns of basis and (Al or Ti) modified Ni/FSM-16 catalysts

the d-spacing of lattices of pore structure were not varied by the Si/Ti ratio.

3.1.2 Normal angle X-ray diffraction

The normal angle XRD pattern of all catalysts are observed in Fig. 2. As obviously, there is a broad peak around $2\theta = 15-30$ due to amorphous silica composing pore walls of FSM-16 [4]. At 2θ above 30, five distinct reflections were observed on XRD patterns of every sample at $2\theta = 37.6$, 43.7, 63.2, 75.8 and 79.6 which were attributed to cubic NiO species (JCPDS no. 44–1159) [44, 45]. Hence, the presence of cubic NiO particles inside the mesoporous structure of FSM-16 as well as Al- and Ti- modified FSM-16 samples were approved. The absence of extra peaks proved that most of Al and Ti metal ions have been either incorporated into the silica framework or their crystallites on the internal or external surface of supports would be too small (< 3 nm) to be detected by X-ray diffraction analysis.

3.1.3 N₂ adsorption/desorption analysis

N₂ sorption isotherms of the synthesized mesoporous supports are illustrated in Fig. 3 and the BET specific surface areas are reported in Table 1. As shown in Fig. 3, the N₂ sorption isotherms of FSM-16 and the Ti and Al modified supports are of IV type in IUPAC classification with an extra hysteresis loops at high relative pressures. This isotherm type belongs to adsorbents with meso-size porous structure [9]. The first hysteresis loop at low relative pressures is of H1 type which presents a step-wise steep increase of N₂ adsorption extending at P/P_0

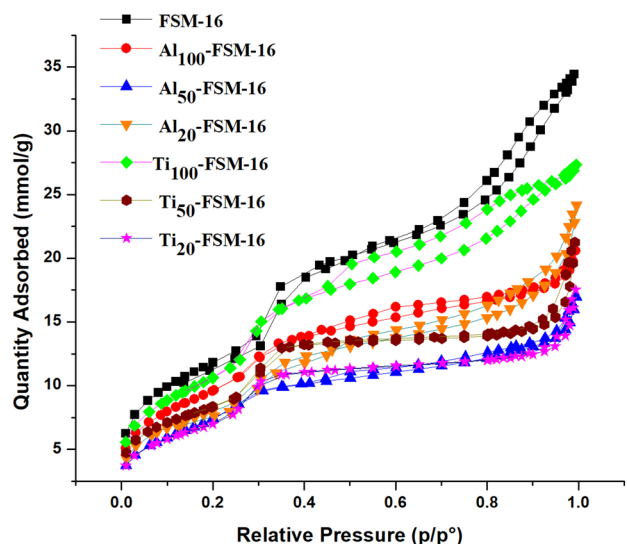


Fig. 3 N₂ Isotherms of FSM-16 and modified mesoporous supports

between 0.15 and 0.5. The H1 hysteresis loop indicates the formation of uniform cylindrical-shape mesopores [46, 47]. Another hysteresis loop of type H₃ at high relative pressures around $P/P_0 \approx 0.55$, suggested the formation of macropores in the void space between the aggregated particles of the samples [48].

The existence of the first H1 hysteresis loop in sorption isotherms of samples indicated that the uniform cylindrical mesopores were formed in all samples [49], however the incorporation of Al and Ti ions in the support structure accompanied with a shift of the adsorption/desorption isotherms to lower values than that of pure FSM-16 support. This downward shift is an evidence of decline of pore volume due to Al/Ti incorporation in the support structure. Increase of Ti incorporation in FSM-16 support resulted in the decrease of mesopore volume up to Si/Ti = 20. D-spacings for all Ti modified supports, given in Table 1, remained constant at 35.7 Å equal to that of FSM-16 support. The mesopore size distribution of the synthesized supports obtained from isotherm adsorption branch data based on BJH model were presented in Fig. 4 and the diameter of mesopores were presented in Table 1. The size of mesopores for Ti modified supports also remained nearly constant below that of FSM-16, except for Ti₅₀-FSM-16 which exhibited a size enlargement. Mesopore volume of Al modified FSM-16 decreased from 0.48 to 0.36 cm³/g with increase of Al content, i.e. from Si/Al ratio = 100–50, followed by a slight recovery of mesopore volume at Si/Al ratio = 20. The size of mesopore showed a continuous decrease with increase of Al content. According to the data in Table 1, d-spacing of support plane (100) of FSM-16 support with

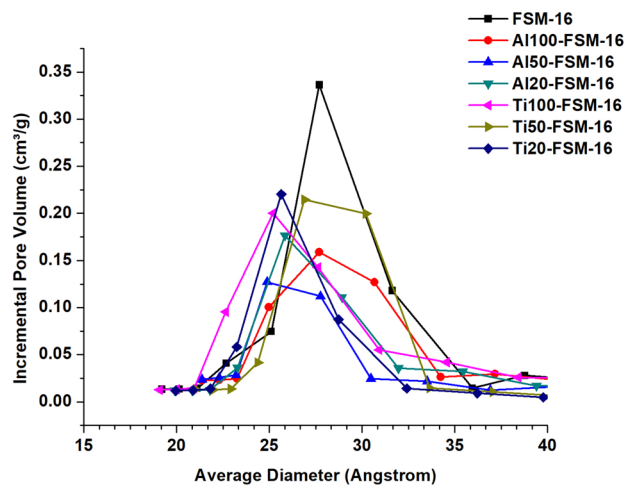


Fig. 4 Mesopore size distribution of the prepared supports obtained from adsorption data based on BJH model

Table 1 Textural properties obtained from N₂ sorption isotherms and XRD patterns

Sample	S _{BET} (m ² /gr)	Mesopore volume (cm ³ /g), d _p <40 Å	D-spacing of planes (100) (Å)	mesopore size ^a (Å)
FSM-16	967	0.61	35.7	27.7
Al ₁₀₀ -FSM-16	786	0.48	35.7	27.7
Al ₅₀ -FSM-16	613	0.36	34.3	26.3
Al ₂₀ -FSM-16	656	0.40	38	25.8
Ti ₁₀₀ -FSM-16	871	0.49	35.7	25.2
Ti ₅₀ -FSM-16	676	0.51	35.7	26.9
Ti ₂₀ -FSM-16	575	0.42	35.7	25.6

^aSize of mesopores with the maximum frequency obtained from BJH PSD

Si/Al = 50 decreased to 34.3 from 35.7 Å for both of FSM-16 and Al₁₀₀-FSM-16 supports, where it increased to 38 Å for the support with Si/Al = 20.

These results could be explained as follows. In the case of Ti modified supports, with the increase of Ti content, the mesopore volumes were nearly fixed but decreased at Ti/Si = 20 most probably due to mesopores mouth blockage by Ti species at this ratio. D-spacing and sizes of mesopores are constant with Ti content. It means that Ti incorporation in the pore wall or deposition inside mesopores is limited and would not be easily increased by increasing Ti content in the synthesis mixture. In the case of Ti₅₀-FSM-16, the mesopore size increased to 26.9 Å while d-spacing and mesopore volume remained close to that of Ti₁₀₀-FSM-16. It could be explained by probable less deposition of Ti species inside mesopores of Ti₁₀₀-FSM-16 due to an unknown reason.

Al incorporation into the structure could take place by the replacement of Si by Al atoms, or extra-framework alumina particle deposition. Considering reducing of D-spacing for Al₅₀-FSM-16, its wall thickness seems to be decreased due to replacement of Si by Al. However, the D-spacing of Al₂₀-FSM-16 increased with further increase of Al incorporation. It seems that extra-framework alumina deposition intensifies as the Al/Si ratio rises. Moreover, the gradual decrease in size of mesopores with Al content could be explained by the deposition of extra-framework deposition of alumina species onto the pore wall.

3.1.4 FTIR spectroscopy

The FTIR spectra of fresh catalysts were presented in Fig. 5a, b. According to the literature [3, 50], two broad and sharp absorption bands around 3450 cm⁻¹ and 1637 cm⁻¹ in Fig. 5a were attributed to stretching vibration of hydroxyl groups and bending vibration, δ(H₂O), of adsorbed water on the support, respectively. For all the catalysts, absorption bands at 1091 cm⁻¹ and 800 cm⁻¹ in Fig. 5b were assigned to Si-O-Si asymmetric and symmetric stretching vibration. A series of Si-O-Si bending vibration appeared in the region of 480–690 cm⁻¹. The weak absorption band centered nearby 970 cm⁻¹ has been assigned to the vibration of defect sites Si-O (=Si-OH) by some researchers [50]. The intensity of this band decreases with the incorporation of higher amount of Al and Ti in the network of Silica FSM-16. Hence, the intensity of band at 970 cm⁻¹ correlates to Al or Ti content, inversely. Furthermore, Ti insertion into the silicate matrix translocated this band to lower wavenumbers, depending on the Ti content. The band shift is larger at the less incorporation level of Ti (Sup. Mat., Figure S1). It may be caused by cancelling effect of neighboring Ti sites at higher Ti/Si ratio on the vibration of associated Si-O bond. Al incorporation into Ni/FSM-16 didn't lead to such a band shift. The bands which appeared at 470 and 445 cm⁻¹ were related to the stretching and bending vibrations of Ni-O.

3.1.5 FESEM analysis of the fresh catalysts

The FESEM technique was applied in order to investigate the morphology of catalyst particles and micrographs of Ni/FSM-16, Ni/Al₅₀FSM-16, and Ni/Ti₁₀₀FSM-16 as depicted in Fig. 6. SEM images of all catalysts are provided in the supplementary data file. SEM images of catalyst particles exhibit no well-defined morphology except for Ni/Al₂₀FSM-16 and to some extent Ni/Ti₂₀FSM-16. Ni/Al₂₀FSM-16 catalyst presented string-like particles. Crystallites of 20–40 nm can be observed in the FESEM images of every catalyst. However, it seems that the number of crystals

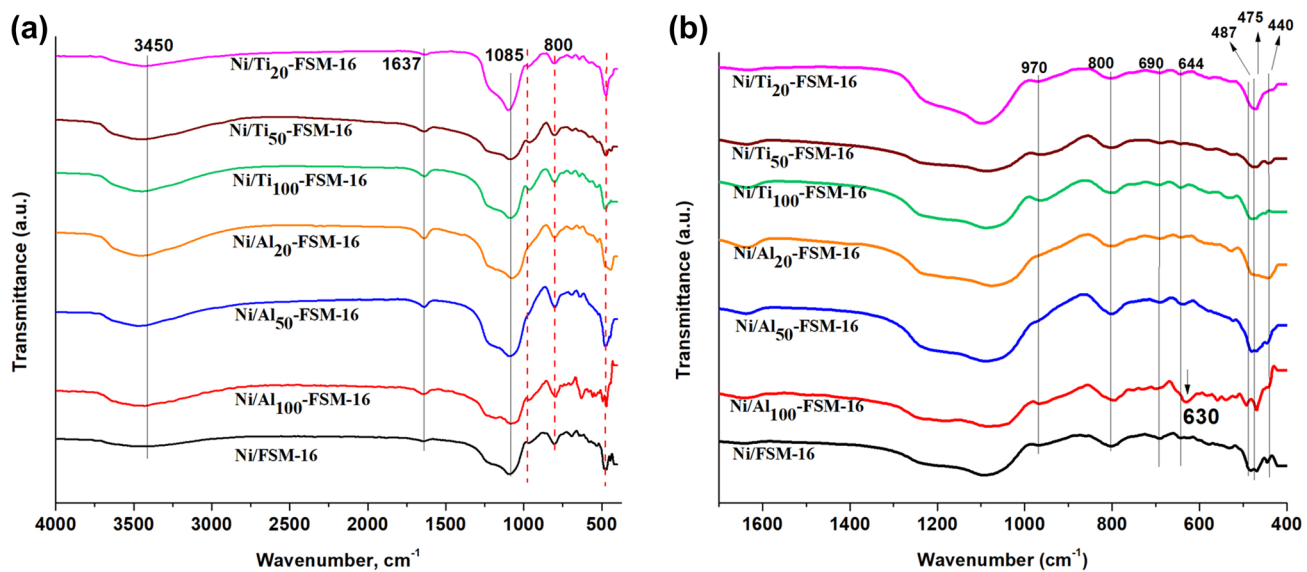


Fig. 5 FT-IR spectra of the prepared Ni/FSM-16, Al, and Ti modified Ni/FSM-16 catalyst, **a** in 4000–400 cm^{-1} range, **b** in 1700–400 cm^{-1} range

of larger size increases with the higher intensity of Al or Ti incorporation into the FSM-16 framework as the support of prepared nickel catalysts. The Al-kanemite crystals with needle-like morphology has been previously reported [51].

3.2 Catalytic performance in dry reforming of methane reaction

The catalytic performance of the prepared catalysts was evaluated at three temperatures (750, 800 and 850 °C) and GHSV ($\text{CH}_4:\text{CO}_2 = 1:1$) h of feed stream of 18,000 (ml/g cat.h) and the activity results were presented in Fig. 7. The highest activities of the catalysts in DRM reaction were obtained at the highest temperature, i.e. 850 °C, where CH_4 and CO_2 conversions and H_2/CO ratio in the product stream were reported in Table 2.

As can be observed in Fig. 7a-b, all the prepared catalysts showed increased conversions of CH_4 and CO_2 with increase in temperature, which is in agreement with chemical equilibrium of DRM reaction as an endothermic conversion. For instance, conversions of CH_4 and CO_2 over Ni/FSM-16 catalyst increased from 37 to 36 % at 750 °C to 47 and 50 % at 850 °C, respectively. Ni-Al₅₀/FSM-16 and Ni-Ti₁₀₀/FSM-16 demonstrated the highest conversion among the Al-modified and Ti-modified FSM-16 supported nickel catalysts, respectively.

In the case of Ni-Al₅₀/FSM-16 catalyst, conversions of CH_4 and CO_2 increased from 65 to 64 % at 750 °C to 84 and 80 % at 850 °C, respectively. The conversions of CH_4 and CO_2 over Ni-Ti₁₀₀/FSM-16 catalyst increased from 45 to 43 % at 750 °C to 71 and 69 % at 850 °C, respectively.

Comparing the catalytic performance of catalysts demonstrated that increase of Al content in the framework of FSM-16 could enhance the catalyst activity in DRM reaction up to Si/Al ratio of 50. Further incorporation of Al in the support framework led to decrease of CH_4 and CO_2 conversions. In the case of Ti-modified catalyst, increase of Ti to Si/Ti ratio of less than 100 resulted in the decline of the conversions of CH_4 and CO_2 .

Each of the Al or Ti modified catalysts presented higher activity than the basis catalyst, i.e. Ni/FSM-16, in DRM with respect to the conversions of CH_4 and CO_2 , except for Ni/Al₂₀-FSM-16 at 750 °C.

According to Fig. 7c, the H_2/CO ratios of the products obtained by all the prepared supported nickel catalysts were less than one, indicating that reverse water gas shift reaction is an active side reaction over the catalysts. The highest value of H_2/CO ratios was also obtained over Ni-Al₅₀/FSM-16 among Al- and Ti- FSM-16 modified supported nickel catalysts. It seems that variation of temperature does not have an intense effect on the H_2/CO ratio of most of the prepared catalysts. However, a decreasing trend of H_2/CO ratio with temperature can be observed for Ni/FSM-16 in contrast to the increasing trend for Ni/Al₅₀-FSM-16. With increasing temperature from 750 to 850 °C, H_2/CO ratio decreased from 0.79 to 0.71 over Ni/FSM-16, whereas it increases from 0.81 to 0.89 by Ni-Al₅₀/FSM-16. RWGS ($\text{H}_2 + \text{CO}_2 \rightleftharpoons \text{CO} + \text{H}_2\text{O}$) and Boudouard reaction ($2\text{CO} \rightleftharpoons \text{C} + \text{CO}_2$) are endothermic and exothermic side reactions, respectively. However, RWGS is kinetically may be less favored at high temperatures than DRM reactions. Therefore, the competence of these reactions could lead to enhancement of H_2/CO

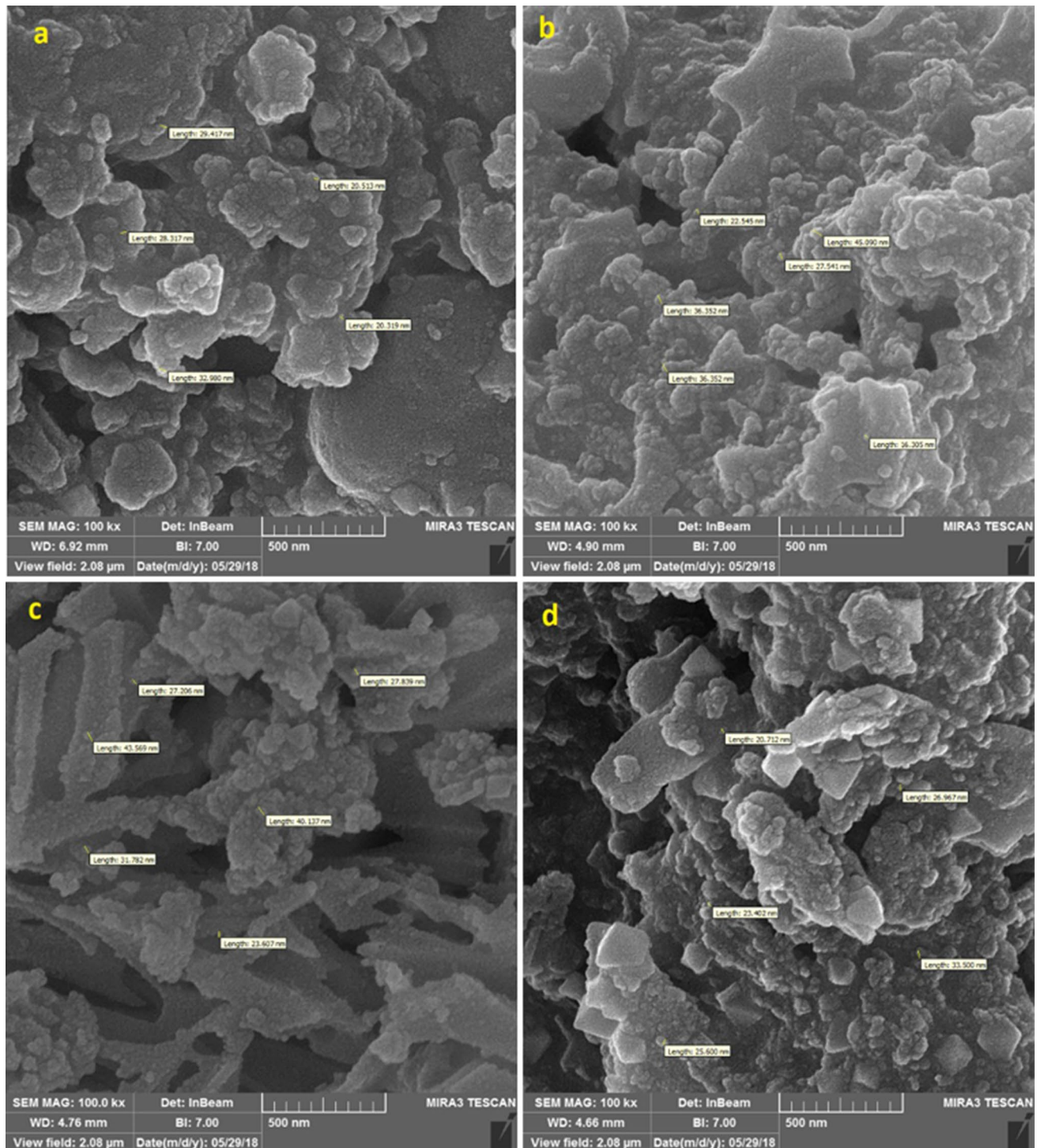


Fig. 6 SEM images of as-prepared catalysts, **a** Ni/FSM-16, **b** Ni/Al₅₀ FSM-16, **c** Ni/Al₂₀ FSM-16, and **d** Ni/Ti₁₀₀ FSM-16

ratio of the products as observed for Ni/Al₅₀-FSM-16. However, at higher temperature the backward Boudouard reaction turns carbon species onto the surface of catalysts to CO faster. It could neutralize or surpass the increasing trend of H₂/CO ratio with temperature. Hence, the effect of backward

Boudouard side reaction can explain the weak decreasing tend of H₂/CO ratio with temperature observed over some of the catalysts, such as Ni/FSM-16 or Ni/Al₁₀₀-FSM-16.

It is noteworthy that H₂/CO ratios of Ni/Ti₂₀-FSM-16 are significantly lower than other catalysts as their values

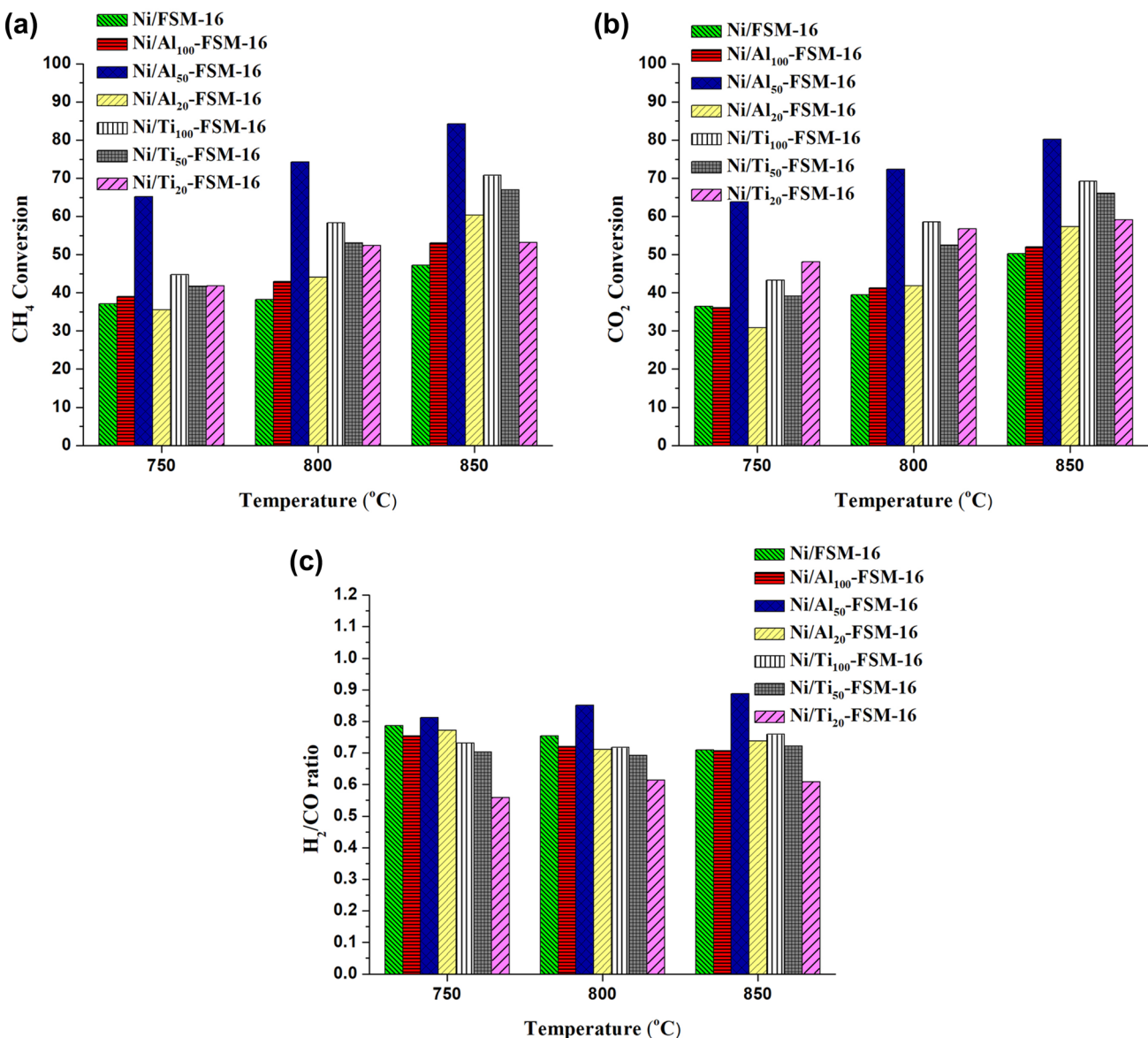
Table 2 Performance of the prepared catalysts in DRM reaction at 850 °C

Catalysts	CH ₄ conver- sion (%)	CO ₂ conver- sion (%)	H ₂ /CO ratio
Ni/FSM-16	47	50	0.71
Ni/Al ₁₀₀ -FSM-16	53	52	0.71
Ni/Al ₅₀ -FSM-16	84	80	0.89
Ni/Al ₂₀ -FSM-16	60	57	0.74
Ni/Ti ₁₀₀ -FSM-16	71	69	0.76
Ni/Ti ₅₀ -FSM-16	67	66	0.72
Ni/Ti ₂₀ -FSM-16	53	59	0.61

are 0.1 to 0.15 less than the nearest H₂/CO ratios which are obtained over Ni/Ti₅₀-FSM-16. Moreover, Ni/Ti₂₀-FSM-16 was the only catalyst that produced water condensed in the steam trap.

According to Fig. 7a–c, it is clear that addition of Al or Ti to FSM-16 as the support of nickel catalyst could enhance the catalytic performance in DRM reaction. For instance, the conversion of CH₄ and CO₂, and H₂/CO ratio of the products of Ni/Al₅₀-FSM-16 catalyst were promoted in the range of 75–95%, 60–83%, 3–25% with respect to Ni/FSM-16 at the different temperatures, respectively.

Results showed that not only the main DRM reaction was promoted at the optimum Si/Al or Si/Ti in the FSM-16

**Fig. 7** DRM Performance for the as-prepared nickel catalyst in different reaction temperatures, GHSV = 18,000 ml/(g.h), CH₄/CO₂ = 1/1 and reaction pressure 1 atm, conversion of **a** CH₄, **b** CO₂, and **c** H₂/CO ratio

structure as the support of Ni catalysts, but also the side reactions, i.e. RWGS and Boudouard, were affected.

At 750 °C, the highest conversion of CH₄ was obtained for catalyst Ni/Al₅₀-FSM-16 in this study. DRM performance of the prepared catalysts is not better than the best results in the literature [52]. For example, a core shell structure of Ni@SiO₂ could convert CH₄ at 72 % at 700 °C [53]. Mesoporous silica or alumina-supported Ni catalyst also resulted in CH₄ conversion of 45–80% [54] [55] [18]. However, Al or Ti incorporation to Silica support can be examined for other catalytic systems such as alumina-supported Ni catalyst for DRM performance promotion.

As displayed in Fig. 8, the modified catalyst Ni/Al₅₀-FSM-16 showed an unstable performance at 750 °C, losing 22 and 27% of initial yield of CO and H₂ after 30 h of time on stream, respectively. Relative molar flow of reactants increased by 5–10 % due to losing activity after 30 h. The increased percentage of CH₄ and CO₂ in the product was less than the decrease of CO and H₂. The imbalance of variations in the reactant and product molar flow rates accounts for the coke formation on the catalyst. Thus, the Al modified FSM-16 supported Ni catalyst with the highest reactant conversion still suffers from rather rapid deactivation.

3.2.1 Temperature programmed reduction (H₂-TPR)

The result of TPR experiments to evaluate the characteristics of metallic Ni particles obtained after reduction of as-prepared nickel catalysts by H₂ are shown in Fig. 9. The TPR profiles can be deconvoluted to four peaks in which their temperature of centerline and areas were calculated

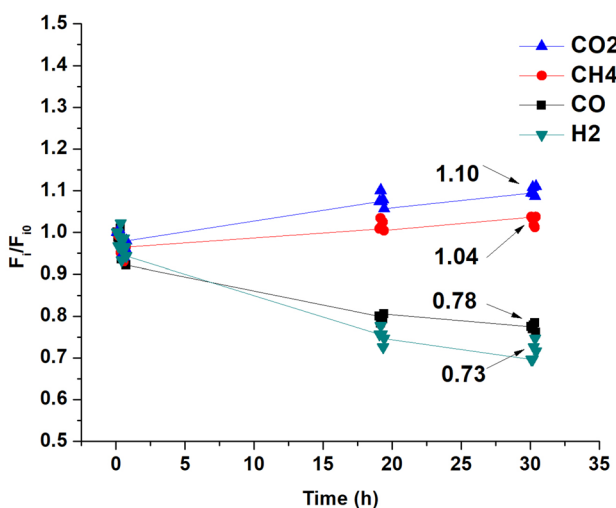


Fig. 8 Stability of Ni/Al₅₀-FSM-16 in DRM reaction at 750 °C, GHSV = 18,000 ml/(g.h), CH₄ /CO₂ = 1/1 and reaction pressure 1 atm: relative molar flow rate of CH₄, CO₂, H₂ and CO

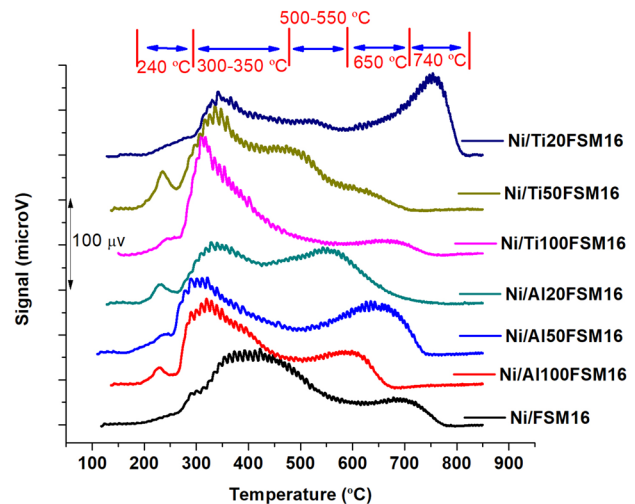


Fig. 9 TPR profiles of the prepared nickel catalysts

and presented in Table S1 and S2 of supplementary material, respectively.

The first peak in TPR profiles 220–270 °C should be related to desorption of adsorbed gas. The latter three peaks are assigned to reduced Ni particles with different levels of interaction with the support. Peak 2 in the TPR profiles, centered in the range of 305–360 °C, was assigned to the nickel particles with the weakest interaction with the support, mostly should be located onto the external surface of the porous structure of catalyst particles. Peak 3 in the TPR profiles is in the 380–530 °C range. These peaks could be related to Ni crystallites with the interaction of medium strength to supports. The last peaks of TPR profiles located in the range of 550–750 °C could be originated from the reduced Ni crystallites with the highest interaction with the support surface.

It is noteworthy that Al incorporated nickel catalyst shows reduction peaks in the smaller range of temperatures with respect to their Ti incorporated catalyst counterparts. It means that Ni crystallites interact stronger to Ti-modified FSM-16 supports than Al-modified ones.

Considering area of reduction peaks, i.e. peaks 2,3,4 in TPR profiles indicated the total Ni content of catalysts are almost comparable.

A study in the variation of the area of peaks and their temperature of centerline showed that the area of the fourth peak of the TPR profile correlates with the CH₄ and CO₂ conversion of the catalyst in the DRM reaction. The larger area of peak 4 in TPR profile with the temperature of the centerline near 627 °C, as the optimum temperature for peak 4, led to higher activity in the corresponding catalyst in DRM reaction.

The second peak in TPR profiles of nickel catalysts related to the nickel crystallites seems not to have a

significant role in the DRM activity of the catalysts. Ni/Ti₅₀-FSM-16 has the largest area of the second peaks but its DRM activity is near to that of Ni/Ti₁₀₀-FSM-16 the area of peak number 2 equals to 50 % of that of the former one. The 4th peak in TPR profile of Ni/Ti₅₀-FSM-16 is of low area but benefits from right temperature leading to drive DRM reaction at a similar rate to that of Ni/Ti₁₀₀-FSM-16 catalyst.

The 3rd peak in TPR profiles of Ni/FSM-16 and Ni/Ti₅₀-FSM-16 catalysts are very similar in terms of both area and temperature of centerline. However, the conversion of CH₄ over these two catalysts shows a difference of as high as 20 %. It indicated the low importance of the third peak in TPR profiles or the Ni crystallite reduced at the temperature relevant to the third peak in DRM activity of these catalysts.

Comparing Ni/Ti₅₀-FSM-16 with the unmodified basis catalyst, shows that the temperature of centerline of the fourth peak in TPR profile is very crucial. The area of the fourth peak for the basis catalyst, Ni/FSM-16, is more than two times of Ni/Ti₅₀-FSM-16, but the activity of Ni/Ti₅₀-FSM-16 is higher than the basis catalyst. The reason is that the temperature of peak center for the basis catalyst is about 50 °C larger than the optimum temperature.

The temperature of centerline of the fourth peak in TPR profile of Ni/Ti₅₀-FSM-16 and Ni/Al₅₀-FSM-16 is the same but the area of the fourth peak for the latter catalyst is 8 times of the former one. The conversion of CH₄ is only 17 % larger than that of Ti₅₀-FSM-16 catalyst. It indicates the stronger effect of temperature of reduction compared to that of quantity of the relevant reduced Ni crystallites. The temperature of reduction reflects the activity of Ni crystallites over which surface Ni atoms with its specific chemical properties drives the DRM reaction. Hence, the optimum temperature of reduction minimizes the energy barrier of the rate determining step of DRM reaction over the relevant Ni crystallites. To show quantitatively the dependence of DRM activity of catalysts on the area and centerline temperature of the 4th TPR peak, several functions of these parameters were examined. A linear correlation, shown in Fig. 10, was found between CH₄ conversion in DRM reaction and a TPR function defined as below.

$$A * ([1 - (T_{C.L.} - 620)] / (800 - 620))^2,$$

where A and T_{C.L.}(°C) are Area and temperature of centerline of the 4th TPR peak, respectively. The stronger effect of temperature of centerline, T_{C.L.}, than area of 4th TPR peak on DRM activity can be inferred from the quadratic relation of the TPR function in terms of T_{C.L.}. It should be noted that the trend lines in Fig. 10 are of different slopes for Al and Ti-modified nickel catalysts. The basis catalyst, Ni/FSM-16, has been placed on the trend line of Al-modified catalysts in Fig. 10. It indicates a different interaction of Ni crystallites

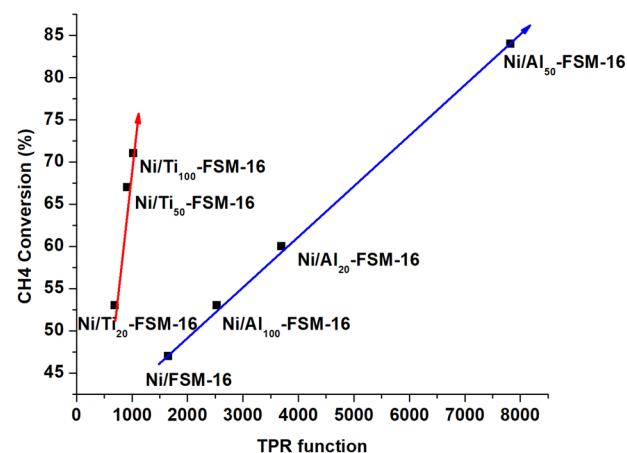


Fig. 10 CH₄ Conversion versus of TPR function

with Ti incorporated FSM-16 support. According to the results of pore volume and size of the prepared catalysts, less incorporation of Ti into the FSM-16 framework compared to Al was pointed out. Hence, it could describe the reason for less effect of incorporation of Ti rather than Al on DRM activity of FSM-16 supported nickel catalyst.

3.3 Characterization of spent catalysts

3.3.1 FTIR spectroscopy

To study the chemical composition of carbon deposited onto the prepared catalysts after DRM reaction, FTIR spectra of used Ni/Al₅₀-FSM-16 and Ni/Ti₁₀₀-FSM-16 as the Al- and Ti-modified catalysts with the highest activity in DRM were obtained. The whole FTIR spectra were displayed in Figure S5 of supplementary material. IR Absorption bands of carbon groups of the above-mentioned catalysts could be analyzed in the wavenumber range of 1600–3100 cm⁻¹, displayed in Fig. 11a, b.

The absorption band around 1630 cm⁻¹ was assigned to C=C stretching vibration, indicating the unsaturated nature of carbon deposits. The C=C bond absorption can be originated from alkenic amorphous coke or graphite.

The FT-IR spectra exhibited C=C absorption band at 1636 and 1627 with small shift with respect to each other. The signal intensity of C=C band stretching vibration of carbon deposits on Ni/Al₅₀-FSM-16 at 1630 cm⁻¹ is clearly stronger than Ni/Ti₁₀₀-FSM-16 at 1627 cm⁻¹.

TPO data, given in Table S4 didn't show a significant difference in the quantity of carbon species formed on these samples after kinetic experiments. Therefore, the intensity difference of the absorption band of C=C bond could probably be due to the coke chemical structure.

Less symmetry of C=C bond caused by substituted alkyl groups in carbon deposits on Ni/Al₅₀-FSM-16 might lead to

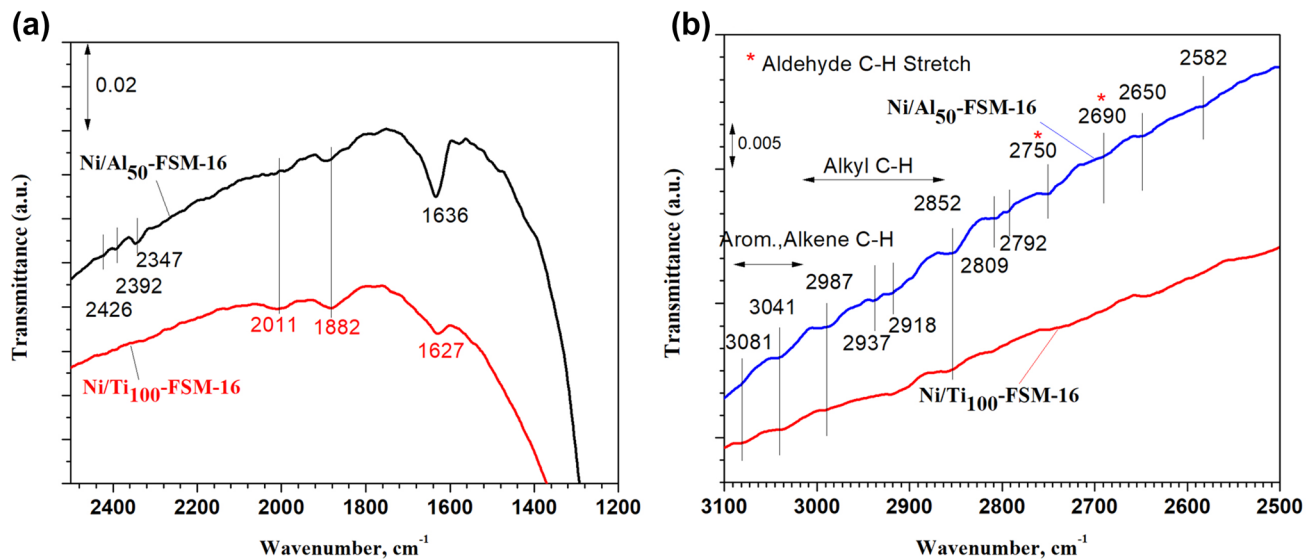


Fig. 11 FT-IR spectra of spent Ni/Al₅₀ FSM-16 and Ni/Ti₁₀₀ FSM-16 catalyst, **a** in 2500–1200 cm⁻¹ range, **b** in 3100–2500 cm⁻¹ range

the observed in both blue shift of vibration frequency and its higher intensity. Bulky alkyl substitute attached to one side of C=C at the border of carbonaceous species domain might slightly weaken the carbon-carbon double bond.

Si-O-Si overtones ($\Delta v > 1$) were found at 1882 and 2011 cm⁻¹ [14]. Two bands observed in Fig. 11 at 2347 and 2392 cm⁻¹ were attributed to C=O asymmetric stretching vibration splitting due to coupling with rotational energy modes in CO₂ [56, 57].

C-H stretching in aliphatic compounds absorbs in the range of 3000–2850 cm⁻¹, while the stretching band of C-H adjacent to a double bond or aromatic ring appears between 3100 and 3000 cm⁻¹ [57].

The FT-IR spectra of the catalysts shown in Fig. 11-b confirmed the presence of CH₂ groups in carbon deposits by exhibiting asymmetric and symmetric –C-H stretching modes at 2937 and 2852 cm⁻¹, respectively. Asymmetric and symmetric -C-H stretching modes in CH₃ groups could be related to absorption in 2987, 2918 cm⁻¹, respectively [58]. Absorption in 3081, 3041 cm⁻¹ could be attributed to -C-H vibration, adjacent to C=C bond, on the border of domain of graphitic coke. This observation suggested the amorphous alkenic or graphitic nature of carbonaceous deposits formed over the spent catalysts.

The Minor absorptions in 2750 and 2690 cm⁻¹ were assigned to Aldehydic C-H stretching absorption frequently appearing in the 2830 to 2695 cm⁻¹ region [57]. The accompanying bending vibration of Aldehydic C-H around 1400 cm⁻¹ and Aldehydic C=O stretching mode near 1740 cm⁻¹ can be observed in the spectra.

It has been widely accepted that CH₄ dissociates in dry reforming of methane leading to CH_x and H species

adsorbed over the surface of Nickel-based catalysts [59]. CO₂ is activated by the resulting adsorbed H leading to OH to which CH_x species reacts and converted to CH_xO species onto the surface of catalyst. It may explain the absorption band of -HC=O (CH_xO, x=1–2) observed in the FTIR spectra of spent samples.

3.4 Temperature programmed oxidation (O₂-TPO)

The characteristics of carbon deposit species over spent nickel catalysts were evaluated via TPO experiment and the TPO profiles were presented in Fig. 12. The TPO profiles could also be deconvoluted to four peaks in which their temperature of centerline and areas were calculated and presented in Table S3 and S4 of supplementary materials, respectively.

The first peak in TPO profiles around 280 °C might be related to the combustion of amorphous carbon deposits. The second TPO peak centered at 430 °C might be assigned to coke species of intermediate state between amorphous and graphitic carbon. The third peak in the TPR profiles, centered about 550 °C, could be ascribed to graphitic carbon deposit. Peak number 4 in the TPR profiles appearing around 695 °C, as the smallest one, might be attributed to the filament or whisker carbon which is responsible for deactivation of the catalyst.

Study of variation of CH₄ conversion versus area of TPO quadruple peaks indicated a significant correlation between the area of the second peak in TPO profiles of the spent catalysts with their DRM activity shown in Fig. 13. The area of other TPO peaks exhibited a reverse relation with the conversion of CH₄. The intermediate state carbon species

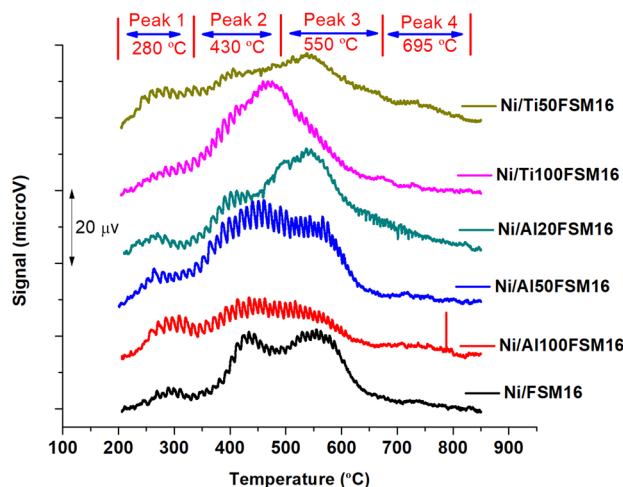


Fig. 12 TPO profiles of the prepared nickel catalysts

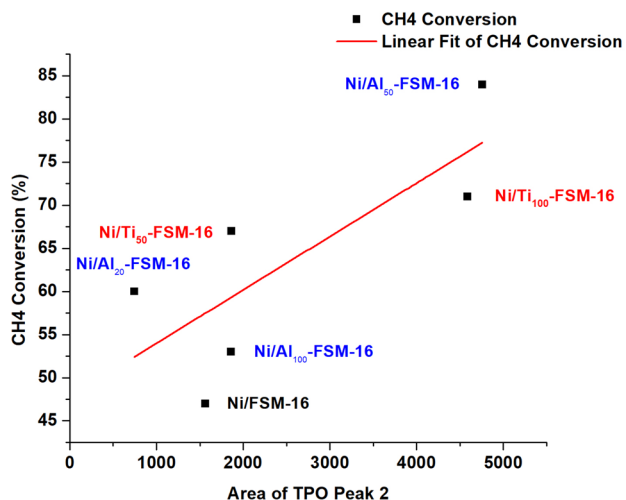


Fig. 13 CH_4 conversion of the prepared nickel catalysts vs. 2nd peak of TPO

giving rise to the 2nd peak in TPO profiles might take apart in the DRM reaction to produce products. Hence, its higher concentration over the prepared catalysts could promote the rate of DRM reaction. From the other hand, other peaks in TPR profiles resulting from other types of carbon species, more resistant to oxidization, correlates inversely to conversion of CH_4 . Therefore, graphitic and whisker coke leading to peak numbers 3 and 4 are inactive in DRM reaction and deactivate the catalyst via blockage of pores mouth or coverage of nickel sites.

It should be noted that part of the area under TPO profiles could be derived from oxidation of crystallites of metallic nickel. However, the rate of nickel oxidation should be much less than the rate of carbonaceous deposit combustion because the former is diffusion limited

especially at low temperature. Therefore, the major part of area of TPO profiles could originate from the combustion of carbon deposits.

Kinetics data demonstrated the significant positive effects of Ti or Al incorporation into FSM-16 framework as the support of nickel catalyst in DRM reaction. Catalyst activity was enhanced at a suitable range of Si/Metal ratio. Side reactions like RWGS and Boudouard were also affected.

TPR results indicated different strengths of nickel interaction with support. It means different sizes of nickel particles have been formed inside the porous structure of FSM-16. XRD data confirmed the presence of NiO crystallites $> 3\text{--}4$ nm with distinct reflections of NiO phase, most probably found on external surface of the catalysts.

However, the obtained correlation of activity data with TPR data revealed that the amount of nickel particles of smallest size (strongest interaction with support) determined the performance of the catalyst in DRM reaction. Al or Ti incorporation into FSM-16 silica led to the formation of a larger number of small Ni particle sizes leading to the higher DRM activity of the catalysts.

Incorporation of aluminum into silica framework produce a negative charge leading to stronger interaction with the cations in impregnating solution. Titanium in silica network might also shift the pH of point of zero charge of silica surface to a higher value leading to promotion of cation capacity of adsorption, although not as strong as that of aluminum.

According to O_2 -TPO results, the total amount of coke didn't change with the modifications of catalysts, though DRM activity was strongly influenced. However, the chemical structure or reactivity of carbonaceous deposit varied with support modification. The more active was the catalyst, the less graphitic coke was formed. Instead, the larger amount of intermediate carbonaceous deposits was formed over more active catalysts. It indicated the carbonaceous deposits with burning temperature around $430\text{ }^\circ\text{C}$ is involved in the mechanism cycle of DRM reaction over nickel catalysts. Therefore, it seems that Ti or Al-modified FM-16 support interacts stronger with NiO crystallites, leading to smaller sized NiO particles with varied chemical properties. The improved chemical property of an NiO and reduced metallic Ni crystallites would affect reaction mechanism, producing more reactive carbon species and higher activity of nickel catalysts.

3.5 Conclusion

The evaluation of the DRM performance of the synthesized nickel catalysts demonstrated a strong effect of incorporation of Al or Ti into FSM-16 silica as the support of catalysts. The high promotion of CH_4 conversion by over 80% was

achieved by Al incorporation. The effect was explained by the increased interaction of nickel particles with the (Al or Ti)-modified FSM-16 silica support material, confirmed by H₂-TPR results. The stronger interaction of nickel particles with the support could lead to smaller particles on the support surface with the varied chemical properties. Carbon species deposited onto the synthesized nickel catalysts of the best performance in DRM reaction showed different oxidation temperatures from which the low temperature-burnt species composed the largest portion. According to O₂-TPO results, the different concentrations of coke species might be evidence of the effect of support modification on the key steps of DRM reaction cycle such as methane decomposition. By employed modification to the support, the higher concentration of carbon species intermediates of higher H/C ratio enhancing the rate of DRM could be expected.

The authors declare that they have no known competing financial interests or personal relationships that could have appeared to influence the work reported in this paper.

Supplementary Information The online version contains supplementary material available at <https://doi.org/10.1007/s10934-021-01111-2>.

Funding Grant of National Strategic Technology Laboratory Network is gratefully acknowledged.

Declarations

Conflict of interest The authors declare that they have no known competing financial interests or personal relationships that could have appeared to influence the work reported in this paper.

References

- M. Usman, W.W. Daud, H.F. Abbas, Dry reforming of methane: influence of process parameters—a review. *Renew. Sustain. Energy Rev.* **45**, 710–744 (2015)
- P. Nikolaidis, A. Poullikkas, A comparative overview of hydrogen production processes. *Renew. Sustain. Energy Rev.* **67**, 597–611 (2017)
- R. Amin, B. Liu, Z.B. Huang, Y.C. Zhao, Hydrogen and syn gas production via CO₂ dry reforming of methane over Mg/La promoted Co–Ni/MSU-S catalyst. *Int. J. Hydrol. Energy* **41**(2), 807–819 (2016)
- J. Goscianska, R. Pietrzak, J. Matos, Catalytic performance of ordered mesoporous carbons modified with lanthanides in dry methane reforming. *Catal. Today* **301**, 204–216 (2018)
- H.S. Whang et al., Enhanced activity and durability of Ru catalyst dispersed on zirconia for dry reforming of methane. *Catal. Today* **293**, 122–128 (2017)
- V. Danghyan, S.C. Novoa, A. Mukasyan, E. Wolf, Pressure dilution, a new method to prepare a stable Ni/fumed silica catalyst for the dry reforming of methane. *Appl. Catal. B* **234**, 178–186 (2018)
- M.M. Nair, S. Kaliaguine, Structured catalysts for dry reforming of methane. *New J. Chem.* **40**(5), 4049–4060 (2016)
- R. Debek, R. Dębek, Novel catalysts for chemical CO₂ utilization. Ph.D. thesis (2016)
- N. Patel, R. Fernandes, S. Gupta, R. Edla, D. Kothari, A. Miotello, Co-B catalyst supported over mesoporous silica for hydrogen production by catalytic hydrolysis of ammonia borane: a study on influence of pore structure. *Appl. Catal. B* **140**, 125–132 (2013)
- W. Li, Z. Zhao, X. Guo, G. Wang, Employing a nickel-containing supramolecular framework as Ni precursor for synthesizing robust supported Ni catalysts for dry reforming of methane. *Chem.-CatChem* **8**(18), 2939–2952 (2016)
- L. Qian et al., Investigation of La promotion mechanism on Ni/SBA-15 catalysts in CH₄ reforming with CO₂. *Fuel* **122**, 47–53 (2014)
- K. Świrk, M.E. Gálvez, M. Motak, T. Grzybek, M. Rønning, P. Da Costa, Syngas production from dry methane reforming over yttrium-promoted nickel-KIT-6 catalysts. *Int. J. Hydrol. Energy* **44**(1), 274–286 (2019)
- S. Zhang, S. Muratsugu, N. Ishiguro, M. Tada, Ceria-doped Ni/SBA-16 catalysts for dry reforming of methane. *ACS Catal.* **3**(8), 1855–1864 (2013)
- S. Qiu, X. Zhang, Q. Liu, T. Wang, Q. Zhang, L. Ma, A simple method to prepare highly active and dispersed Ni/MCM-41 catalysts by co-impregnation. *Catal. Commun.* **42**, 73–78 (2013)
- Z. Roosta, A. Izadbakhsh, A. Sanati, S. Osfouri, Synthesis and evaluation of NiO@MCM-41 core–shell nanocomposite in the CO₂ reforming of methane. *J. Porous Mater.* **25**(4), 1135–1145 (2018)
- E.N. Alvar, M. Rezaei, “Mesoporous nanocrystalline MgAl₂O₄ spinel and its applications as support for Ni catalyst in dry reforming.” *Scr. Mater.* **61**(2), 212–215 (2009)
- N. Hadian, M. Rezaei, Combination of dry reforming and partial oxidation of methane over Ni catalysts supported on nanocrystalline MgAl₂O₄. *Fuel* **113**, 571–579 (2013)
- M. Rezaei, S.M. Alavi, S. Sahebdelfar, L. Xinmei, L. Qian, Z.-F. Yan, “CO₂ – CH₄ reforming over nickel catalysts supported on mesoporous nanocrystalline zirconia with high surface area. *Energy Fuels* **21**(2), 581–589 (2007)
- D. Liu, X.Y. Quek, W.N.E. Cheo, R. Lau, A. Borgna, Y. Yang, MCM-41 supported nickel-based bimetallic catalysts with superior stability during carbon dioxide reforming of methane: effect of strong metal–support interaction. *J. Catal.* **266**(2), 380–390 (2009)
- E. Lovell et al., CO₂ reforming of methane over MCM-41-supported nickel catalysts: altering support acidity by one-pot synthesis at room temperature. *Appl. Catal. A* **473**, 51–58 (2014)
- X. Zhang et al., “Nickel nanoparticles embedded in mesopores of AISBA-15 with a perfect peasecod-like structure: a catalyst with superior sintering resistance and hydrothermal stability for methane dry reforming.” *Appl. Catal. B* **224**, 488–499 (2018)
- C.-Y. Chen, S.-Q. Xiao, M.E. Davis, Studies on ordered mesoporous materials III. Comparison of MCM-41 to mesoporous materials derived from kanemite. *Microporous Mater.* **4**(1), 1–20 (1995)
- S. Inagaki, FSM-16 and mesoporous organosilicas. *Stud. Surf. Sci. Catal.* **148**, 109–132 (2004)
- T. Kimura, K. Kuroda, Ordered mesoporous silica derived from layered silicates. *Adv. Func. Mater.* **19**(4), 511–527 (2009)
- T. Linssen, K. Cassiers, P. Cool, E. Vansant, Mesoporous templated silicates: an overview of their synthesis, catalytic activation and evaluation of the stability. *Adv. Colloid Interface Sci.* **103**(2), 121–147 (2003)
- D.T. On, D. Desplantier-Giscard, C. Danumah, S. Kaliaguine, Perspectives in catalytic applications of mesostructured materials. *Appl. Catal. A* **222**, 1–2 (2001)
- Y. Kitayama, H. Asano, T. Kodama, J. Abe, Y. Tsuchiya, Synthesis of Sn-incorporated folded sheets mesoporous materials (Sn-FSM-16). *J. Porous Mater.* **5**(2), 139–146 (1998)

28. Y. Liu, T. Hanaoka, K. Murata, K. Okabe, I. Takahara, K. Sakanishi, Synthesis of Zr-containing FSM-16 as an effective support for Co catalyst in the Fischer-Tropsch synthesis. *React. Kinet. Catal. Lett.* **92**(1), 147–154 (2007)
29. T. Selvam, M. Köstner, G. Mabande, W. Schwieger, N. Pfänder, R. Schlögl, Synthesis, characterization and catalytic properties of mesoporous Al-FSM-16 materials. *J. Porous Mater.* **14**(3), 263–272 (2007)
30. M. Zimowska et al., A comparative study of direct versus post-synthesis alumination of mesoporous FSM-16 silica. *Mater. Res. Bull.* **83**, 623–631 (2016)
31. B.A. Mehrabadi, S. Eskandari, U. Khan, R.D. White, J.R. Regalbuto, A review of preparation methods for supported metal catalysts. *Adv. Catal.* **61**, 1–35 (2017)
32. Y. Shu, L.E. Murillo, J.P. Bosco, W. Huang, A.I. Frenkel, J.G. Chen, The effect of impregnation sequence on the hydrogenation activity and selectivity of supported Pt/Ni bimetallic catalysts. *Appl. Catal. A* **339**(2), 169–179 (2008)
33. J.R. Sietsma et al., Ordered mesoporous silica to study the preparation of Ni/SiO₂ ex nitrate catalysts: impregnation, drying, and thermal treatments. *Chem. Mater.* **20**(9), 2921–2931 (2008)
34. M. Cabo et al, Influence of the preparation method on the morphology of templated NiCo₂O₄ spinel. *J. Nanopart. Res.* **13**(9), 3671–3681 (2011)
35. L. Guo-Min, W. Lian-Cheng, X. Yao, Templated synthesis of highly ordered mesoporous cobalt ferrite and its microwave absorption properties. *Chin. Phys. B* **23**(8), 088105 (2014)
36. I. Lopes, N.El Hassan, H. Guerba, G. Wallez, A. Davidson, Size-induced structural modifications affecting Co₃O₄ nanoparticles patterned in SBA-15 silicas. *Chemistry of materials* **18**(25), 5826–5828 (2006)
37. J. van der Meer, I. Bardez, F. Bart, P.-A. Albouy, G. Wallez, A. Davidson, Dispersion of Co₃O₄ nanoparticles within SBA-15 using alkane solvents. *Microporous Mesoporous Mater.* **118**, no. 1–3 (2009) pp. 183–188
38. J. Van Der Meer, I. Bardez-Giboire, C. Mercier, B. Revel, A. Davidson, R. Denoyel, Mechanism of metal oxide nanoparticle loading in SBA-15 by the double solvent technique. *J. Phys. Chem. C* **114**(8), 3507–3515 (2010)
39. M. Kaydouh, N. El Hassan, A. Davidson, S. Casale, H.El Zakhem, P. Massiani, Highly active and stable Ni/SBA-15 catalysts prepared by a “two solvents” method for dry reforming of methane. *Microporous Mesoporous Mater.* **220**, 99–109 (2016)
40. M. Tao, Z. Xin, X. Meng, Y. Lv, Z. Bian, Impact of double-solvent impregnation on the Ni dispersion of Ni/SBA-15 catalysts and catalytic performance for the syngas methanation reaction. *RSC Adv.* **6**(42), 35875–35883 (2016)
41. S. Inagaki, Y. Fukushima, Adsorption of water vapor and hydrophobicity of ordered mesoporous silica, FSM-16. *Microporous Mesoporous Mater.* **21**, no. 4–6 (1998) pp. 667–672
42. A. Matsumoto, T. Sasaki, N. Nishimiya, K. Tsutsumi, Thermal stability and hydrophobicity of mesoporous silica FSM-16. *Colloids Surf., A* **203**, no. 1–3 (2002) pp. 185–193
43. Z. Taherian, M. Yousefpour, M. Tajally, B. Khoshandam, Promotional effect of samarium on the activity and stability of Ni-SBA-15 catalysts in dry reforming of methane. *Microporous Mesoporous Mater.* **251**, 9–18 (2017)
44. S. Damyanova, B. Pawelec, K. Arishtirova, J. Fierro, C. Sener, T. Dogu, MCM-41 supported PdNi catalysts for dry reforming of methane. *Appl. Catal. B* **92**, 3–4 (2009)
45. S. Qiu, Q. Zhang, W. Lv, T. Wang, Q. Zhang, L. Ma, Simply packaging Ni nanoparticles inside SBA-15 channels by co-impregnation for dry reforming of methane. *RSC Advances* **7**(39), 24551–24560 (2017)
46. S. Inagaki, Y. Fukushima, K. Kuroda, Synthesis and characterization of highly ordered mesoporous material; FSM-16, from a layered polysilicate. *Stud. Surf. Sci. Catal.* **84**, 125–132 (1994)
47. S. Inagaki, A. Koizumi, N. Suzuki, Y. Fukushima, K. Kuroda, Syntheses of highly ordered mesoporous materials, FSM-16, derived from kanemite. *Bull. Chem. Soc. Jpn.* **69**(5), 1449–1457 (1996)
48. C. Galacho, M.R. Carrott, P. Carrott, Evaluation of the thermal and mechanical stability of Si-MCM-41 and Ti-MCM-41 synthesised at room temperature. *Microporous Mesoporous Mater.* **108**, no. 1–3 (2008) pp. 283–293
49. H. Xia, B. Liu, Q. Li, Z. Huang, A.S.-C. Cheung, High capacity Mn-Fe/Mo/FSM-16 sorbents in hot coal gas desulfurization and mechanism of elemental sulfur formation. *Appl. Catal. B* **200**, 552–565 (2017)
50. M.S. Ghattas, Cobalt-modified mesoporous FSM-16 silica: Characterization and catalytic study. *Microporous Mesoporous Mater.* **97**, no. 1–3 (2006) pp. 107–113
51. D.L. Guerra, C. Airolidi, Thermochemical data for n-alkylmonoamines functionalization into lamellar silicate Al-kanemite. *J. Chem. Thermodyn.* **43**(1), 69–74 (2011)
52. F. Gholizadeh, A. Izadbakhsh, J. Huang, Y. Zi-Feng, Catalytic performance of cubic ordered mesoporous alumina supported nickel catalysts in dry reforming of methane. *Microporous Mesoporous Mater.* **310**, 110616 (2021)
53. C. Wang et al., The importance of inner cavity space within Ni@SiO₂ nanocapsule catalysts for excellent coking resistance in the high-space-velocity dry reforming of methane. *Appl. Catal. B* **259**, 118019 (2019)
54. L. Xu, H. Zhao, H. Song, L. Chou, Ordered mesoporous alumina supported nickel based catalysts for carbon dioxide reforming of methane. *Int. J. Hydrog. Energy* **37**(9), 7497–7511 (2012)
55. A.H. Fakirha, S.O. Kasim, A.A. Ibrahim, A.E. Abasaeed, A.S. Al-Fatesh, Influence of nature support on methane and CO₂ conversion in a dry reforming reaction over nickel-supported catalysts. *Materials* **12**(11), 1777 (2019)
56. K. Coenen, F. Gallucci, B. Mezari, E. Hensen, M. van Sint, Anna-land, An in-situ IR study on the adsorption of CO₂ and H₂O on hydrotalcites. *J. CO₂ Utilization* **24**, 228–239 (2018)
57. B. Stuart, Infrared spectroscopy. In: Kirk-Othmer encyclopedia of chemical technology. Wiley, New York (2000)
58. F.X.W. Robert, M. Silverstein, D.J. Kiemle, D.L. Bryce, Spectrometric Identification of Organic Compounds. State University of New York, New York (2015)
59. J. Gao, Z. Hou, H. Lou, X. Zheng, Dry (CO₂) reforming. Fuel cells: technologies for fuel processing. Elsevier, New York, pp. 191–221 (2011)

Publisher's Note Springer Nature remains neutral with regard to jurisdictional claims in published maps and institutional affiliations.